Draft version October 13, 2015
Preprint typeset using LaTeX style emulateapj v. 5/2/11

arXiv:1510.03343v1 [astro-ph.CO] 12 Oct 2015

PLASMA INSTABILITIES IN THE CONTEXT OF CURRENT HELIUM SEDIMENTATION MODELS: DYNAMICAL IMPLICATIONS FOR THE ICM IN GALAXY CLUSTERS

Thomas Berlok and Martin E. Pessah
Niels Bohr International Academy, Niels Bohr Institute, Blegdamsvej 17, 2100 Copenhagen, Denmark
Draft version October 13, 2015

ABSTRACT

Understanding whether Helium can sediment to the core of galaxy clusters is important for a number of problems in cosmology and astrophysics. All current models addressing this question are one-dimensional and do not account for the fact that magnetic fields can effectively channel ions and electrons, leading to anisotropic transport of momentum, heat, and particle diffusion in the weakly collisional intracluster medium (ICM). This anisotropy can lead to a wide variety of instabilities, which could be relevant for understanding the dynamics of heterogeneous media. In this paper, we consider the radial temperature and composition profiles as obtained from a state-of-the-art Helium sedimentation model and analyze its stability properties. We find that the associated radial profiles are unstable, to different kinds of instabilities depending on the magnetic field orientation, at all radii. The fastest growing modes are usually related to generalizations of the Magnetothermal Instability (MTI) and the Heat-flux-driven Buoyancy Instability (HBI) which operate in heterogeneous media. We find that the effect of sedimentation is to increase (decrease) the predicted growth rates in the inner (outer) cluster region. The unstable modes grow fast compared to the sedimentation timescale. This suggests that the composition gradients as inferred from sedimentation models, which do not fully account for the anisotropic character of the weakly collisional environment, might not be very robust. Our results emphasize the subtleties involved in understanding the gas dynamics of the ICM and argue for the need of a comprehensive approach to address the issue of Helium sedimentation beyond current models.

Subject headings: galaxies: clusters: intracluster medium — instabilities — magnetohydrodynamics — diffusion

1. INTRODUCTION

Galaxy clusters are important astrophysical probes since their masses can be used to constrain cosmological parameters (Mantz et al. 2014 and references therein). The distribution of mass as a function of radius can be inferred by modeling the observed X-ray emission produced by Bremsstrahlung in the hot intracluster medium (ICM). The intensity of the emission depends on the radial distribution of temperature and density, as well as the composition of the gas. While the temperature of the ICM is reasonably well determined (Vikhlinin et al. 2006), the composition of the plasma is not. The reason is that many of the elements are completely ionized at the characteristic temperatures of the ICM and thus their abundances cannot be directly inferred. Therefore, the interpretation of the X-ray data normally relies on assuming a model for the composition of the gas. A widely adopted approximation consists on assuming the composition of the plasma to be uniform (see Bulbul et al. 2011 for an analysis where this assumption is relaxed). Elements heavier than hydrogen are expected to sediment over cosmological timescales (Fabian & Pringle 1977), therefore the assumption of a homogeneous ICM relies on this process being inefficient. Turbulence and tangled magnetic fields, or a combination of both, have been invoked as potential agents (Markevitch 2007).

Even though the mass ratio between Helium (He) and Hydrogen (H) is small, because He is the most abundant of the heavy elements, it has the potential to induce significant variations in the mean molecular weight. If He sedimentation does take place and this is not accounted for when modeling galaxy clusters, this could induce biases in the cosmological parameters derived (Qin & Wu 2000; Markevitch 2007; Peng & Nagai 2009). This could prove to be a problem for precision cosmology and highlights the importance of understanding the distribution of heavy elements in the ICM (Fabian & Pringle 1977; Gilfanov & Syunyaev 1984; Chuzhoy & Nusser 2003; Chuzhoy & Loeb 2004; Peng & Nagai 2009; Shtykovskiy & Gilfanov 2010a). Most of the previous work on this subject is based on solving Burgers' equations for a multicomponent plasma (Burgers 1969; Thoul et al. 1994) and all of these assume spherical symmetry in order to predict the composition of the ICM as a function of radius. Studies addressing the long term evolution of the composition of the ICM have considered the dynamical effects of magnetic fields in a rather crude way, usually encapsulating their effects in a parameter that regulates the slow down of the sedimentation process (Peng & Nagai 2009).

A more recent, and somewhat parallel, line of developments has helped us realize that the dynamical properties of magnetized, weakly collisional, stratified plasmas can be rather subtle. Balbus (2000, 2001) and Quataert (2008) showed that stratified plasmas that are stable according to the Schwarzschild criterion could turn unstable due to the presence of a magnetic field, even if its strength is too weak to be mechanically important. The plasma can become unstable because even a very weak magnetic field can effectively alter transport processes by channeling electrons and ions, leading to anisotropic heat conduction and Braginskii viscosity (Braginskii 1965; Kunz 2011).

berlok@nbi.dk

Previous studies have considered plane-parallel, fully ionized *homogeneous* atmospheres with a temperature gradient in the direction of gravity. In this setting there are two instabilities that feed on the gradient in temperature. The Magnetothermal Instability (MTI) has the fastest growth rate when the magnetic field is perpendicular to gravity and the temperature decreases with height (Balbus 2000, 2001). The Heat-flux-driven Buoyancy Instability (HBI) has the fastest growth rate when the magnetic field is parallel to gravity and the temperature increases with height (Quataert 2008). Because of the temperature profiles observed in typical cool-core galaxy clusters (Vikhlinin et al. 2006), the MTI is believed to be active in the outer parts of the ICM while the HBI is believed to be relevant in the inner parts of the ICM. These instabilities have been studied extensively in the literature both analytically (Balbus 2000, 2001; Quataert 2008; Kunz 2011; Latter & Kunz 2012) and numerically with initially local simulations with anisotropic heat conduction (Parrish & Stone 2005, 2007; Parrish & Quataert 2008) and since then with elaborate physical models (Parrish et al. 2008, 2009; Bogdanović et al. 2009; Parrish et al. 2010; Ruszkowski & Oh 2010; McCourt et al. 2011, 2012; Kunz et al. 2012; Parrish et al. 2012a,b).

The aforementioned works that deal with the weakly collisional character of the magnetized plasma have usually adopted a homogeneous atmosphere as a model for the ICM. On the other hand, the sedimentation models are usually one-dimensional and do not fully account for dynamical properties of the magnetic field. In an effort to better understand the interplay between the Helium distribution in the ICM and its weakly collisional and weakly magnetized nature, Pessah & Chakraborty (2013) considered the presence of a gradient in the Helium composition and extended previous stability criteria. Their work shows that a gradient in composition can modify the stability properties of a stratified atmosphere. This could have consequences for the Helium sedimentation models which could be unstable to plasma instabilities.

The equations used to model the plasma in Pessah & Chakraborty (2013) describe the stability properties of a weakly collisional plasma subject to a background composition gradient, but they do not account for the process of Helium sedimentation which is estimated to occur on longer timescales.[1] Because of this, the equations are thus unable to predict how a gradient in composition arises from an initial homogeneous plasma. A framework that simultaneously considers the physics responsible for Helium sedimentation together with the anisotropic transport properties governing dilute, magnetized plasmas has yet to be developed. A key goal for the future is therefore to develop such a model in order to determine from first principles the rate at which Helium can sediment in a weakly collisional, magnetized medium. In lieu of such a fully consistent theory, this paper has a more modest goal. Our aim is to understand the kind of instabilities, and their associated timescales and length scales, that can feed off the temperature and composition profiles that emerge from state-of-the-art models for Helium sedimentation in the ICM (Peng & Nagai 2009; Shtykovskiy & Gilfanov 2010a).

The rest of the paper is organized as follows. In Section 2, we introduce the equations that we use to model the weakly collisional three-component plasma. In Section 3, we derive an extended version of the dispersion relation presented by Pessah & Chakraborty (2013) to account for the effects of magnetic tension, which can be important in cluster cores. In Section 4, we discuss the stability criteria for atmospheres with temperature and composition gradients. In Section 5, we solve the dispersion relation for isothermal atmospheres in order to gain insight into the type of instabilities that can be excited solely by composition gradients. In Section 6, we consider the temperature and composition gradients derived from the Helium sedimentation model of Peng & Nagai (2009). By allowing the background magnetic field to have an arbitrary inclination with respect to gravity we identify the most relevant instabilities in different regions of the ICM. Finally, we conclude by discussing future prospects for addressing the problem of Helium sedimentation in galaxy clusters on more fundamental grounds in Section 7.

[1] We discuss the limitations of this work in this regard in Appendix A.1.

2. THE EQUATIONS OF KINETIC MHD FOR A BINARY MIXTURE

The kinetic MHD equations for a fully ionized binary mixture of Hydrogen and Helium can be written as (Pessah & Chakraborty 2013)

$$\frac{\partial \rho}{\partial t} + \boldsymbol{\nabla}\cdot(\rho \boldsymbol{v}) = 0\,, \tag{1}$$

$$\frac{\partial (\rho \boldsymbol{v})}{\partial t} + \boldsymbol{\nabla}\cdot\left(\rho \boldsymbol{v}\boldsymbol{v} + P_{\rm T}\mathbf{I} - \frac{B^2}{4\pi}\hat{\boldsymbol{b}}\hat{\boldsymbol{b}}\right) = -\boldsymbol{\nabla}\cdot\Pi + \rho \boldsymbol{g}, \tag{2}$$

$$\frac{\partial \boldsymbol{B}}{\partial t} = \boldsymbol{\nabla}\times(\boldsymbol{v}\times\boldsymbol{B})\,, \tag{3}$$

$$\frac{\rho T}{\mu}\frac{ds}{dt} = -\boldsymbol{\nabla}\cdot\boldsymbol{Q}_{\rm s} - \Pi\!:\!\boldsymbol{\nabla}\boldsymbol{v}\,, \tag{4}$$

$$\frac{dc}{dt} = -\boldsymbol{\nabla}\cdot\boldsymbol{Q}_{\rm c}\,. \tag{5}$$

Here, the Lagrangian and Eulerian derivatives are related via $d/dt = \partial/\partial t + \boldsymbol{v}\cdot\nabla$, ρ is the mass density, $\boldsymbol{v}$ is the fluid velocity, $\boldsymbol{g} = (0, 0, -g)$ is the gravitational acceleration and $\mathbf{I}$ stands for the 3×3 identity matrix. The symbols $\perp$ and $\parallel$ refer respectively to the directions perpendicular and parallel to the magnetic field $\boldsymbol{B}$ whose direction is given by the unit vector $\hat{\boldsymbol{b}} = \boldsymbol{B}/B = (b_x, 0, b_z)$. The total pressure is $P_{\rm T} = P + B^2/8\pi$, where P is the thermal pressure, and the entropy per unit mass is defined by

$$s = \frac{3k_{\rm B}}{2m_{\rm H}} \ln\left(P\rho^{-5/3}\right)\,, \tag{6}$$

where $k_{\rm B}$ is Boltzmann's constant and $m_{\rm H}$ is the proton mass. The adiabatic index, γ, has been set to $5/3$ in the preceding equations and throughout the remainder of the paper.

The composition of the plasma, c, is defined to be the ratio of the Helium density to the total gas density

$$c = \frac{\rho_{\rm He}}{\rho_{\rm H} + \rho_{\rm He}}\,. \tag{7}$$

The associated mean molecular weight, μ, influences the dynamics of the plasma through the equation of state

$$P = \frac{\rho k_{\rm B} T}{\mu m_{\rm H}}\,, \tag{8}$$

where T is the temperature. We assume a completely ionized plasma consisting of Helium and Hydrogen and the mass

concentration of Helium, c, is therefore related to the mean molecular weight, μ, by

$$\mu = \frac{4}{8-5c} \,. \tag{9}$$

The evolution of the binary mixture is influenced by three different non-ideal effects, namely Braginskii viscosity, which is described through the viscosity tensor (Braginskii 1965)

$$\Pi = -3\rho\nu_{\parallel}\left(\hat{\boldsymbol{b}}\hat{\boldsymbol{b}} - \frac{1}{3}\mathbf{I}\right)\left(\hat{\boldsymbol{b}}\hat{\boldsymbol{b}} - \frac{1}{3}\mathbf{I}\right) : \boldsymbol{\nabla v} \,, \tag{10}$$

anisotropic heat conduction described by the heat flux (Spitzer 1962; Braginskii 1965)

$$\boldsymbol{Q}_s = -\chi_{\parallel}\hat{\boldsymbol{b}}\hat{\boldsymbol{b}} \cdot \nabla T, \tag{11}$$

and anisotropic diffusion of Helium described by the composition flux

$$\boldsymbol{Q}_c = -D\hat{\boldsymbol{b}}\hat{\boldsymbol{b}} \cdot \nabla c \,. \tag{12}$$

The transport coefficients ($\chi_{\parallel}$, $\nu_{\parallel}$, and D) all depend on the temperature, as well as the composition of the plasma. The dependences are given in Appendix B by Equations (B6), (B7) and (B8), respectively. For more details on the kinetic MHD approximation and its limitations see the relevant discussions in Schekochihin et al. (2005), Kunz et al. (2012), Pessah & Chakraborty (2013) and references therein.

3. THE DISPERSION RELATION

We consider an initially motionless, plane-parallel atmosphere with gradients in both temperature and the mean molecular weight. A local linear mode analysis of this atmosphere, using Equations (1)–(5) and following the procedure in Pessah & Chakraborty (2013), leads to the dispersion relation

$$\sum_{i=0}^{4} A_i + \omega_{\rm v} \sum_{i=1}^{5} B_i = 0 \,, \tag{13}$$

where the coefficients are given by

$$A_0 = \sigma^2\tilde{\sigma}^4 k^2 \,, \tag{14}$$

$$A_1 = \sigma\tilde{\sigma}^4 \left(\omega_D + \omega_c\right) k^2 \,, \tag{15}$$

$$A_2 = \sigma^2\tilde{\sigma}^2 N^2 \left(k_x^2 + k_y^2\right) + \tilde{\sigma}^4\omega_c\omega_D k^2 \,, \tag{16}$$

$$A_3 = \sigma\tilde{\sigma}^2 g\omega_c \left\{\frac{d\ln T}{dz}\mathcal{K} - \frac{d\ln\mu}{dz}\left(k_x^2 + k_y^2\right)\right\} + \sigma\tilde{\sigma}^2\omega_D N^2\left(k_x^2 + k_y^2\right) \,, \tag{17}$$

$$A_4 = \tilde{\sigma}^2\omega_c\omega_D N_{T/\mu}^2 \mathcal{K} \,, \tag{18}$$

$$B_1 = \sigma^3\tilde{\sigma}^2 k_{\perp}^2 \,, \tag{19}$$

$$B_2 = \sigma^2\tilde{\sigma}^2 \left(\omega_D + \omega_c\right) k_{\perp}^2 \,, \tag{20}$$

$$B_3 = \sigma^3 b_x^2 k_y^2 N^2 + \sigma\tilde{\sigma}^2\omega_c\omega_D k_{\perp}^2 \,, \tag{21}$$

$$B_4 = \sigma^2 b_x^2 k_y^2 \left(N_{T/\mu}^2\omega_c + N^2\omega_D\right) \,, \tag{22}$$

$$B_5 = \sigma b_x^2 k_y^2 N_{T/\mu}^2 \omega_c\omega_D \,. \tag{23}$$

Here, $k_{\parallel} = \hat{\boldsymbol{b}}\cdot\boldsymbol{k}$ and $k_{\perp}^2 = k^2 - k_{\parallel}^2$ and we have defined

$$\omega_{\rm c} = \frac{2}{5}\frac{\chi_{\parallel}T}{P}k_{\parallel}^2 \,, \quad \omega_{\rm v} = 3\nu_{\parallel}k_{\parallel}^2 \,, \quad \omega_{\rm D} = Dk_{\parallel}^2 \,, \tag{24}$$

which are the inverse timescales associated with anisotropic heat conduction, viscosity and particle diffusion. Furthermore, we have introduced the quantity

$$\mathcal{K} = \left(1 - 2b_z^2\right)\left(k_x^2 + k_y^2\right) + 2b_x b_z k_x k_z \,, \tag{25}$$

as well as the Brunt−Väisälä frequency, N, such that

$$N^2 = \frac{2}{5}\frac{m_{\rm H}}{k_{\rm B}} g\frac{ds}{dz} \,, \tag{26}$$

and the quantity

$$N_{T/\mu}^2 = g\frac{d}{dz}\ln\left(\frac{T}{\mu}\right) . \tag{27}$$

The effects of magnetic tension, which are neglected in Pessah & Chakraborty (2013) and could be important in the inner parts of the ICM (Carilli & Taylor 2002), are contained in

$$\tilde{\sigma}^2 = \sigma^2 + \omega_{\rm A}^2 \,, \tag{28}$$

where

$$\omega_{\rm A} = k_{\parallel}v_{\rm A} \,, \tag{29}$$

is the Alfvén frequency and $v_{\rm A} = B/\sqrt{4\pi\rho}$ is the Alfvén velocity.

3.1. *Characteristic Scales and Dimensionless Variables*

There are a number of characteristic scales that are useful to introduce. The dynamical frequency, $\omega_{\rm dyn}$, is given by

$$\omega_{\rm dyn} = \sqrt{\frac{g}{H}} \,, \tag{30}$$

where H is the thermal pressure scale height and g is the gravitational acceleration. We will use that hydrostatic equilibrium requires

$$g\frac{d\ln P}{dz} = -\omega_{\rm dyn}^2 \,. \tag{31}$$

The plasma-β, given by the ratio of the thermal velocity and the Alfvén speed squared $\beta = v_{\rm th}^2/v_{\rm A}^2$, where $v_{\rm th}^2 = P/\rho$, provides a measure of the strength of the magnetic field.

We also define the Knudsen number

$$\mathrm{Kn} = \frac{\lambda_{\rm mfp}}{H} \,, \tag{32}$$

which is a measure of the collisionality of the plasma. Here, $\lambda_{\rm mfp}$ is the mean-free-path of ion collisions. Intuitively, $\mathrm{Kn}^{-1} = H/\lambda_{\rm mfp}$ is the average number of collisions an ion experiences as it traverses a distance of one scale height. So $\mathrm{Kn}^{-1} \gg 1$ ($\mathrm{Kn}^{-1} \ll 1$) corresponds to high (low) collisionality. As in Pessah & Chakraborty (2013), we define an effective ion-ion collision frequency

$$\nu_{ii}^{\rm eff} = \frac{v_{\rm th}^2}{2\nu_{\parallel}} \,, \tag{33}$$

which can be used to express the inverse Knudsen number as

$$\mathrm{Kn}^{-1} = \frac{\nu_{ii}^{\rm eff}}{\omega_{\rm dyn}} \,, \tag{34}$$

by using that $\lambda_{\rm mfp} = v_{\rm th}/\nu_{ii}^{\rm eff}$.

In Section 5, it will prove useful to use a dimensionless form of the theory and present the results in terms of variables that have been scaled using the characteristic time provided by $\omega_{\rm dyn}^{-1}$ and the characteristic length given by $(\lambda_{\rm mfp}H)^{1/2}$. In order to accomplish this, we assume that the inverse timescales for heat conduction and Braginskii viscosity are related to the dynamical frequency via (Kunz 2011)

$$\omega_{\rm c} \simeq 10 k_\parallel^2 \lambda_{\rm mfp} H \omega_{\rm dyn} \,, \tag{35}$$

$$\omega_{\rm v} \simeq \frac{3}{2} k_\parallel^2 \lambda_{\rm mfp} H \, \omega_{\rm dyn} \,. \tag{36}$$

When diffusion of Helium is included in the analysis we furthermore assume that

$$\omega_{\rm D} \simeq \frac{1}{4} k_\parallel^2 \lambda_{\rm mfp} H \, \omega_{\rm dyn} \,. \tag{37}$$

The approximations given by Equations (35)-(37) are justified in Appendix A.2.

Note that the local linear analysis leading to the dispersion relation in Pessah & Chakraborty (2013) is only valid when the wavenumbers involved satisfy the inequalities

$$\sqrt{\rm Kn} \ll k_\parallel (\lambda_{\rm mfp} H)^{1/2} \ll \sqrt{\rm Kn^{-1}} \,, \tag{38}$$

$$\frac{1}{10\sqrt{\beta \rm Kn}} \ll k_\parallel (\lambda_{\rm mfp} H)^{1/2} \ll \sqrt{\beta \rm Kn} \,. \tag{39}$$

The dispersion relation in Equation (13) is also valid even when the inequality given by Equation (39) is not fulfilled because the effects of magnetic tension, which are proportional to the product βKn in dimensionless variables, are included in its derivation. The dispersion relation is, however, still only adequate for describing scales that are both much longer than the mean-free-path of ion collisions (the fluid limit) and much shorter than the scale height of the atmosphere considered (the local limit). The modes of interest therefore need to fulfill Equation (38).

In the resulting dimensionless variables the gradients in the temperature and the mean molecular weight enter as $d\ln T/d\ln P$ and $d\ln\mu/d\ln P$, making it easier to compare the results of this paper with previous work (Pessah & Chakraborty 2013).

4. STABILITY PROPERTIES

The stability criterion for a stratified *collisional* atmosphere is known as the Schwarzschild criterion (Schwarzschild 1958). According to this criterion, the plasma is stable if the entropy increases with height, z, i.e., if

$$\frac{ds}{dz} > 0 \,. \tag{40}$$

If the atmosphere is stratified in temperature and composition, the criterion determining the stability of the atmosphere becomes

$$\frac{d\ln T/\mu}{d\ln P} < \frac{2}{5} \,. \tag{41}$$

This is the Ledoux criterion known from stellar convection theory (Ledoux 1947). Isothermal atmospheres with

$$\frac{d\ln\mu}{d\ln P} > -\frac{2}{5} \,, \tag{42}$$

are therefore stable according to the Ledoux criterion. On the other hand, atmospheres with a uniform composition need to fulfill

$$\frac{d\ln T}{d\ln P} < \frac{2}{5} \,. \tag{43}$$

If Equation (41) is not fulfilled a fluid element that is perturbed upwards (downwards) will expand (contract) and continue to rise (sink). We will refer to this type of instability as gravity modes.

Atmospheres that satisfy the Ledoux criterion for stability (which assumes that the plasma is collisional) are seen to be unstable when transport processes are anisotropic in a weakly collisional plasma. When anisotropic heat conduction is taken into account, isothermal atmospheres with $-2/5 < d\ln\mu/d\ln P < 0$ are unstable regardless of the magnetic field inclination with respect to gravity. When anisotropic particle diffusion is considered even atmospheres with $d\ln\mu/d\ln P > 0$ can become unstable.

The analysis carried out in Pessah & Chakraborty (2013) shows that there are a host of instabilities that can feed off temperature and composition gradients (see their Figures 2 and 4 for an overview of their results). Here, we focus our attention on the instabilities that have the dominant growth rates for the cluster model of Peng & Nagai (2009) in the regime in which heat conduction is fast with respect to the dynamical timescale, i.e., $\omega_{\rm c} \gg \omega_{\rm dyn}$. For convenience, we summarize here some of the most relevant features of these instabilities:

1. The Magneto-thermo-compositional Instability (MTCI) has its fastest growth rate when the magnetic field is perpendicular to the direction of gravity. In the limit of a weak magnetic field the MTCI stability criterion is

$$\frac{d\ln\mu/T}{d\ln P} > 0 \quad \text{if } b_x \neq 0 \,. \tag{44}$$

   As pointed out in Pessah & Chakraborty (2013), this criterion for stability is not affected by anisotropic particle diffusion. This feature of the MTCI is explained in further detail in Section 5.2.1.

2. The Heat- and Particle-flux-driven Buoyancy Instability (HPBI) has its fastest growth rate when the magnetic field is parallel to the direction of gravity. If we ignore particle diffusion and magnetic field tension, the HPBI stability criterion is

$$\frac{d\ln\mu T}{d\ln P} > 0 \quad \text{if } b_z \neq 0,\ \omega_{\rm D} \ll \omega_{\rm dyn} \,. \tag{45}$$

   Note that, even if this criterion is fulfilled, overstable modes might be present, see Equation (57) in Pessah & Chakraborty (2013).

3. The diffusive HPBI, which depends on anisotropic diffusion of particles, has its fastest growth rate when the magnetic field is parallel to the direction of gravity. The diffusive HPBI ($\omega_{\rm D} \neq 0$) has a stability criterion which is qualitatively different from the non-diffusive HPBI ($\omega_{\rm D} = 0$). The criterion for stability for the diffusive HPBI is

$$\frac{d\ln T/\mu}{d\ln P} > 0 \quad \text{if } b_z \neq 0,\ \omega_{\rm D} \gg \omega_{\rm dyn} \,. \tag{46}$$

4. A type of instability driven by anisotropic diffusion of Helium, which we refer to as diffusion modes, also depend on $\omega_D \neq 0$. Diffusion modes have their fastest growth rate when the magnetic field is parallel to the direction of gravity. The stability criterion for diffusion modes is[2]

$$\left|\frac{d\ln T}{d\ln P}\right| > \left|\frac{d\ln \mu}{d\ln P}\right| \quad \text{if } b_z \neq 0,\ \omega_D \neq 0\ . \tag{47}$$

When the mean molecular weight is constant, Equation (44) reduces to the stability criterion for the MTI and Equations (45) and (46) both reduce to the stability criterion for the HBI. These instabilities, driven by thermal gradients in weakly collisional, homogeneous plasmas, have been studied in great detail (Balbus 2000, 2001; Parrish & Stone 2005, 2007; Parrish & Quataert 2008; Parrish et al. 2008; Quataert 2008; Kunz 2011; Kunz et al. 2012; Latter & Kunz 2012; Parrish et al. 2012a).

Before considering the instabilities that are present when the temperature and composition gradients are those obtained from current sedimentation models, we consider a series of simpler cases in order to build our intuition.

5. APPLICATION TO ISOTHERMAL ATMOSPHERES

In order to shed light on the instabilities that are driven by composition gradients we focus our attention on the case of isothermal atmospheres in which the mean molecular weight increases with height. For these atmospheres, the stability criteria for the HPBI and the MTCI, Equations (45) and (44), both reduce to $d\ln\mu/d\ln P > 0$. In the following we analyze simple magnetic field geometries and assume, for simplicity, that the magnetic field strength is negligible and thus $\omega_A = 0$. In this section, we calculate the growth rates associated with axisymmetric modes as a function of the wavenumbers k_x and k_z. Here, k_x is the wavenumber perpendicular to gravity and k_z is the wavenumber parallel to gravity. The latter corresponds to the radial direction in the ICM. We relate our results to the findings of Kunz (2011) who analyzed the MTI and the HBI in detail.

5.1. *Isothermal Atmospheres with No Particle Diffusion*

We solve the dispersion relation, Equation (13), for an isothermal atmosphere with a gradient in composition in the limit where diffusion of particles is neglected ($\omega_D = 0$).

5.1.1. *Magnetic Field Perpendicular to Gravity*

We start out by considering the configuration where the MTCI is maximally unstable, namely a horizontal magnetic field, i.e., $b_x = 1$. We consider an atmosphere with $d\ln\mu/d\ln P = -1/3$. This atmosphere is stable according to the Ledoux criterion, Equation (42), which means that it would be stable if the plasma were collisional. It is however unstable according to the MTCI criterion that applies in the weakly collisional regime.

There is an interesting correspondence between the MTI and MTCI, which is useful in order to make connections with previous results. In order to illustrate this, let us ignore particle diffusion of He ($\omega_D = 0$). In this case, the dispersion relation given by Equation (13) only depends on the gradients in temperature and mean molecular weight through the combination $d\ln(T/\mu)/d\ln P$. This means that the dispersion relation for the MTCI at constant temperature with $d\ln\mu/d\ln P = -1/3$, is identical to the dispersion relation for the MTI with $d\ln T/d\ln P = 1/3$. The crucial difference is of course that in the former case the instabilities are driven by the temperature gradient, whereas in the latter case they are driven by the composition gradient.

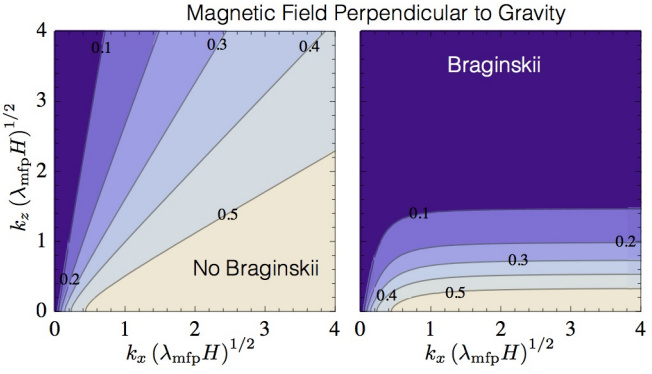

Figure 1. Contour plots of $\sigma/\omega_{\rm dyn}$ for the MTCI with $d\ln\mu/d\ln P = -1/3$ without (left) and with Braginskii viscosity (right). Because of the similarity between the MTI and the MTCI these figures are similar to Figure 5 in Kunz (2011).

The correspondence between MTI and MTCI is illustrated in Figure 1, where we show the growth rate of unstable modes when $d\ln\mu/d\ln P = -1/3$ and obtain a similar result as Kunz (2011) did for the MTI with $d\ln T/d\ln P = 1/3$. In the left panel of Figure 1, Braginskii viscosity is not included and the maximum growth rate has $k_z = 0$. The maximum growth rate of $\sigma/\omega_{\rm dyn} = 0.5$ is confined to a wedge in wavenumber space with $k_z \lesssim 0.5k_x$. In the right panel of Figure 1, Braginskii viscosity is included and the growth rate of $\sigma/\omega_{\rm dyn} = 0.5$ is now confined to a thin band with $k_z(\lambda_{\rm mfp}H)^{1/2} \lesssim 0.3$. We observe that the growth rates are only significant when $k_z(\lambda_{\rm mfp}H)^{1/2} \ll k_x(\lambda_{\rm mfp}H)^{1/2}$. This preference for parallel wavenumbers ($k_{\rm max} \approx k_\parallel$, where $k_{\rm max}$ is the wavenumber for $\sigma_{\rm max}$) is thoroughly investigated by Kunz (2011). Due to the identical dispersion relations for the MTI and the MTCI at constant temperature, we therefore refer to Equations (62) (without Braginskii viscosity) and (64) (with Braginskii viscosity) in Kunz (2011) for approximate limits on the magnitude of $k_\perp$ above which the growth rates become negligible.

5.1.2. *Magnetic Field Parallel to Gravity*

Next, we consider the case of $b_z = 1$, i.e., a vertical magnetic field, where the HPBI is maximally unstable. The growth rate for the HPBI as a function of wavenumber is shown in Figure 2 for the case of $d\ln\mu/d\ln P = -1$.

In the left panel of Figure 2, Braginskii viscosity is not included and the large growth rates are confined to $k_z \lesssim k_x$. In the right panel of Figure 2, Braginskii viscosity is included and the preference for $k_\perp \gg k_\parallel$ is increased. The growth rate of $\sigma/\omega_{\rm dyn} = 0.8$ is now confined to $0.05 \lesssim k_z(\lambda_{\rm mfp}H)^{1/2} \lesssim 0.3$. We conclude that the HPBI favors wavenumbers that have a large perpendicular component and that the available wavenumber space is a narrow band with $k_\perp \gg k_\parallel$ when Bra-

[2] There is a typo in the text below Equation (63) in Pessah & Chakraborty (2013) where the stability criterion is missing an absolute value sign acting on the left hand side of the inequality. This typo does not affect any conclusions or figures in their paper.

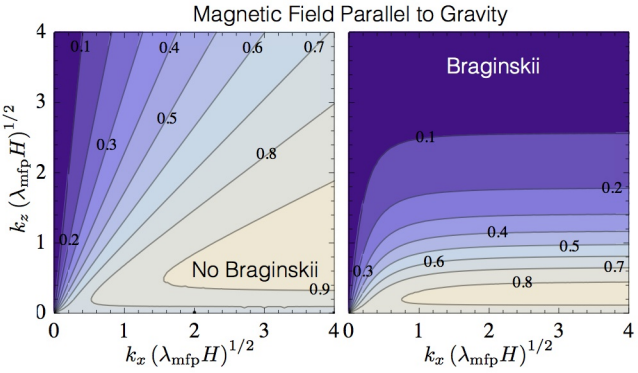

Figure 2. Contour plots of $\sigma/\omega_{\rm dyn}$ for the HPBI with $d\ln\mu/d\ln P = -1$ without (left) and with Braginskii viscosity (right). The qualitative behavior is similar to the HBI but the maximum growth rates are located at smaller $k_z(\lambda_{\rm mfp}H)^{1/2}$. Gravity modes are seen at low $k_z(\lambda_{\rm mfp}H)^{1/2}$.

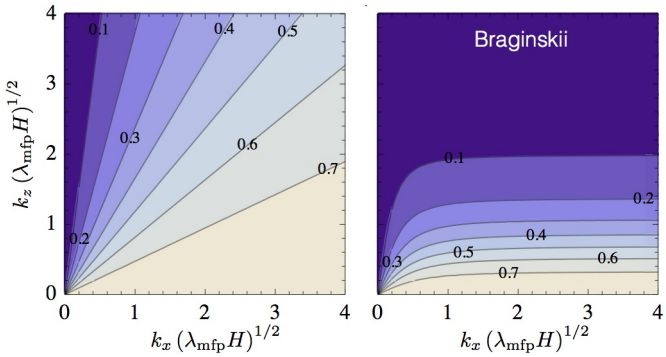

Figure 3. Contour plots of $\sigma/\omega_{\rm dyn}$ for gravity modes with $d\ln\mu/d\ln P = -1$ which appear even without anisotropic transport. *Left:* Without Braginskii viscosity and the growth rate of gravity modes is independent of the magnetic field inclination. *Right:* With Braginskii viscosity and the gravity modes with $k_z(\lambda_{\rm mfp}H)^{1/2} \gtrsim 2$ have negligible growth rate due to damping by Braginskii viscosity. The damping depends on the magnetic field inclination which is taken to be $\theta = 90°$.

ginskii viscosity is included in the analysis.

Figure 2 looks remarkably similar to the corresponding figure for the HBI (with $d\ln T/d\ln P = -1$) presented in Kunz (2011) but they are not identical at low $k_z(\lambda_{\rm mfp}H)^{1/2}$. Even though the HBI and HPBI both have the property that $\sigma = 0$ for $k_\parallel = 0$ we observe that $\sigma/\omega_{\rm dyn} \approx 0.7$ along the line of $k_\parallel = 0$ in both the left and right panels of Figure 2. The explanation is that gravity modes are unstable for different signs of the logarithmic derivatives of T and μ, as seen in Equations (42) and (43). The growth rate of gravity modes for $d\ln\mu/d\ln P = -1$ at these wavenumbers has the value $\sigma/\omega_{\rm dyn} \approx 0.7$. The reason for gravity modes at low $k_z(\lambda_{\rm mfp}H)^{1/2}$ is that heat conduction is too slow to drive the HPBI when $k_\parallel$ is small. The gravity modes do not depend on heat conduction and they are therefore dominant in this slow conduction limit.

The gravity modes are not seen at high $k_z(\lambda_{\rm mfp}H)^{1/2}$ because they are damped by Braginskii viscosity. Even though the HPBI is also damped by Braginskii viscosity, the HPBI turns out to have a higher growth rate than the gravity modes at high $k_z(\lambda_{\rm mfp}H)^{1/2}$. Gravity modes are present even in the absence of anisotropic transport, as illustrated in the left panel of Figure 3. The damping of gravity modes by Braginskii viscosity is demonstrated in the right panel of Figure 3.

An important conclusion in Kunz (2011) is that the local mode analysis for the HBI is not strictly valid when Braginskii viscosity is taken into account because the largest growth rates are obtained for $k_\parallel < H^{-1}$, implying that Equation (38) is not satisfied. The HPBI has its maximum growth rate at even longer wavelengths than for the HBI and we therefore reach a similar conclusion for the HPBI at constant temperature as Kunz (2011) did for the HBI. A quasi-global model has been developed for the HBI by Latter & Kunz (2012). This kind of approach can also be generalized to develop quasi-global models including composition gradients.

5.1.3. *More General Magnetic Field Geometries*

In this section, we explore the consequences of the presence of a magnetic field which is inclined at an angle θ with respect to the horizontal. The components of $\hat{\boldsymbol{b}}$ are thus given by $b_x = \cos\theta$ and $b_z = \sin\theta$. In the previous two sections, and in agreement with Kunz (2011), we showed that Braginskii viscosity can play a significant role in the growth of modes driven by composition gradients. Therefore, we include both anisotropic heat conduction and Braginskii viscosity in our analysis.

We consider an atmosphere with $d\ln\mu/d\ln P = -1$ which is maximally unstable to the MTCI when $\theta = 0°$ and to the HPBI when $\theta = 90°$. Figure 4 shows the unstable modes that emerge as the inclination of the magnetic field is varied, increasing from $\theta = 0°$ in the leftmost panel to $\theta = 90°$ in the rightmost panel. The directions of $\boldsymbol{k} = \boldsymbol{k}_\parallel$ and $\boldsymbol{k} = \boldsymbol{k}_\perp$ are indicated with a red solid line and a red dashed line, respectively. In the previous sections we argued that the MTCI has its maximum growth rate for wavenumbers with $k_\parallel \gg k_\perp$ while the HPBI has its maximum growth rate for $k_\perp \gg k_\parallel$. This provides an intuitive way to interpret Figure 4 which illustrates that the isothermal atmosphere is unstable regardless of the magnetic field inclination, θ.

The results displayed in Figure 4 can be analyzed further with the insights gained earlier in this section. Only the MTCI is unstable in the first panel ($\theta = 0°$) and the most unstable wavenumbers lie in a band along $k_z = k_\perp = 0$. In the second panel, this unstable band is rotated to lie along $\theta = 30°$, which is the angle of $\boldsymbol{k}_\parallel$ with respect to the horizontal. At the same time, a new unstable band has appeared in the direction $\boldsymbol{k} = \boldsymbol{k}_\perp$. This is the HPBI which prefers $k_\perp \gg k_\parallel$. We note again that both the MTCI and the HPBI have zero growth rate along $k_\parallel = 0$ (the dashed line) and so the growth rates seen along this line must be due to gravity modes.

In the third panel ($\theta = 45°$), both unstable bands have rotated by another 15 degrees. The maximum growth rate of the HPBI (MTCI) unstable band has increased (decreased) to $\sigma/\omega_{\rm dyn} = 0.6$ ($\sigma/\omega_{\rm dyn} = 0.7$). The maximum growth rate is found in a region around $k_z = 0$ and it difficult to associate this wavenumber with a specific instability. In the fourth panel ($\theta = 75°$), the maximum growth rate of the HPBI unstable band has increased even further and it is now larger than the maximum growth rate of the MTCI whose growth rate has decreased down to $\sigma/\omega_{\rm dyn} = 0.3$. In the final panel ($\theta = 90°$), the MTCI is completely stabilized and only the modes associated with the HPBI remain.

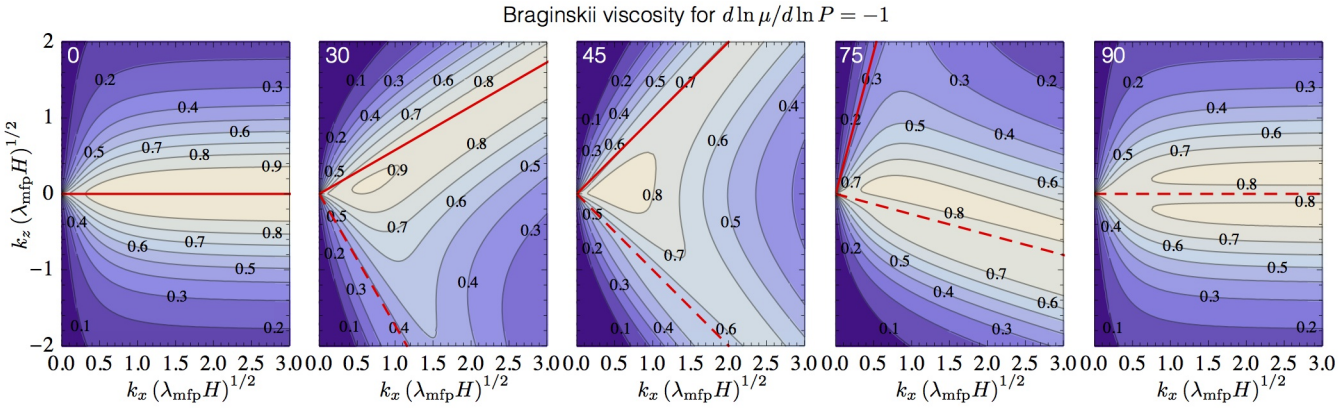

Figure 4. Contour plots of $\sigma/\omega_{\rm dyn}$ for an isothermal atmosphere with $d\ln\mu/d\ln P = -1$, with Braginskii viscosity. The red solid line indicates $k = k_\parallel$ and the red dashed line indicates $k_\parallel = 0$. The MTCI has its maximum growth rate for $k = k_\parallel$ and the HPBI has its maximum growth rate with a small parallel component ($k \gg k_\parallel$). The inclination of the magnetic field is written in degrees at the top, left corner in each panel.

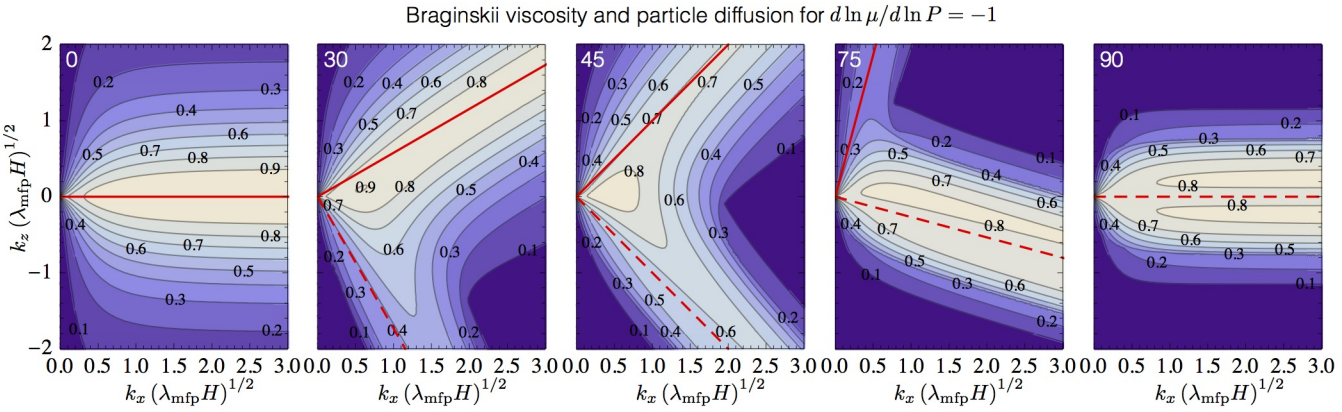

Figure 5. Contour plots of $\sigma/\omega_{\rm dyn}$ for an isothermal atmosphere with $d\ln\mu/d\ln P = -1$, with Braginskii viscosity and particle diffusion. The red solid line indicates $k = k_\parallel$ and the red dashed line indicates $k_\parallel = 0$. The inclination of the magnetic field is written in degrees at the top, left corner in each panel. From left to right: The MTCI at constant temperature is weakened as the magnetic field becomes more vertical. It has its fastest growing modes along $k = k_\parallel$. The slow diffusion modes and the diffusive HPBI are maximally unstable when the magnetic field is vertical. They are visible from the second figure and onwards. In the last figure the field is entirely vertical and the MTCI is stabilized. The instabilities that remain are the slow diffusion modes, the diffusive HPBI and the gravity modes.

5.2. *Diffusion of Helium*

In this section, we consider the stability properties of a weakly collisional, weakly magnetized, binary plasma with Braginskii viscosity and anisotropic diffusion of particles. We focus our attention on isothermal atmospheres that are stratified in composition.

5.2.1. *An Atmosphere with $d\ln\mu/d\ln P = -1$*

We start out by considering an atmosphere with $d\ln\mu/d\ln P = -1$ which is unstable to gravity modes. When the effect of anisotropic diffusion of He is ignored, this atmosphere is generally unstable to both the MTCI and the HPBI, as shown in the previous section. In this section diffusion of particles is included in the analysis.

The anisotropic diffusion of He enables a number of new processes (Pessah & Chakraborty 2013). First and foremost, a new type of instabilities, termed diffusion modes, appear. These modes only exist due to anisotropic diffusion of Helium and their growth rate increase with the value of the diffusion coefficient, D. Second, a new type of instability, termed the diffusive HPBI (Pessah & Chakraborty 2013) appears in place of the HPBI when $\omega_{\rm D} \gg \omega_{\rm dyn}$.

The stability criterion for the MTCI is unaffected by the presence of particle diffusion, as seen in Equations (60) and (68) in Pessah & Chakraborty (2013). The fact that the stability criterion of the MTCI is unaffected can be understood intuitively by considering a fluid parcel moving upwards in a gravitational potential while being connected to its previous surroundings by a magnetic field line. The vertical displacement of the parcel gives rise to an expansion of the parcel. In the the absence of heat transfer to the parcel this expansion would lead to a decrease in the temperature. Due to anisotropic heat conduction, however, the magnetic field line is effectively an isotherm. The parcel is therefore heated from below, rendering it unstable. This mechanism for instability is the same as for the MTI but with the mean molecular weight playing the role of the temperature in the background atmosphere. The mean molecular weight is initially constant along the field line and it is unaffected by expansions or contractions of the fluid parcel. The vertical displacement does therefore not give rise to any anisotropic particle diffusion along the field line and we conclude that the MTCI should be largely unaffected by $D \neq 0$.

The new features enabled by particle diffusion are illustrated in Figure 5, which only differs from Figure 4 in that

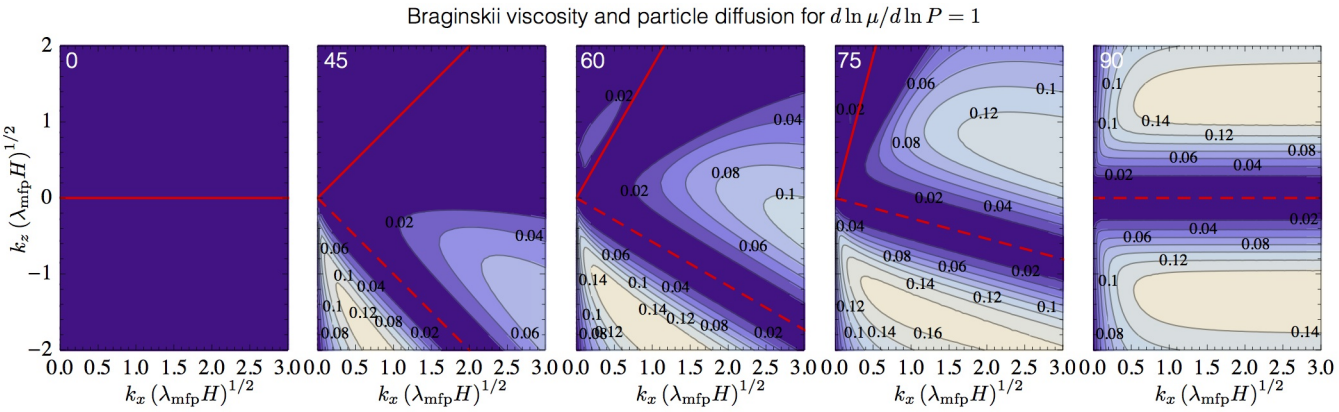

Figure 6. The diffusion modes for $d\ln\mu/d\ln P = 1$. This instability is driven by diffusion of He and is only unstable when $D \neq 0$ and $b_z \neq 0$. The diffusion mode with $d\ln\mu/d\ln P = 1$ operates on a smaller length scale than the diffusion mode with $d\ln\mu/d\ln P = -1$.

particles are able to diffuse along magnetic field lines, i.e., $\omega_{\rm D} = k_\parallel^2 \lambda_{\rm mfp} H \omega_{\rm dyn}/4$. The first and leftmost panels of Figure 4 and 5 are identical because the MTCI is mostly unaffected by particle diffusion, as explained above. The second panel shows the MTCI unstable band along $\boldsymbol{k}_\parallel$ and the diffusion modes along $\boldsymbol{k}_\perp$. In the third panel, where the magnetic field is inclined at 45 deg, there is a region of stability between the two bands of unstable modes. This is in stark contrast with the third panel of Figure 4 where the corresponding region has significant growth rates. The fifth and rightmost panel of Figure 5 can be roughly divided into two unstable bands: An inner band with a growth rate of $\sigma/\omega_{\rm dyn} = 0.7$ and an outer band with a maximum growth rate of $\sigma/\omega_{\rm dyn} = 0.2$. The inner band has the same growth rate as the gravity modes seen in the fifth panel of Figure 4 and the second panel of Figure 2. The maximum growth rate of $\sigma/\omega_{\rm dyn} = 0.8$ is confined to a small area of wavenumber space. Furthermore, we see that a large region of wavenumber space is stable when particle diffusion is included. We conclude that the instabilities have an even stronger tendency to prefer $k_\perp \gg k_\parallel$ when particle diffusion is included.

5.2.2. *An Atmosphere with $d\ln\mu/d\ln P = 1$*

Next, we consider an atmosphere with $d\ln\mu/d\ln P = 1$. This atmosphere is only unstable when anisotropic diffusion of particles is taken into account. Furthermore, the unstable modes require that the magnetic field has a vertical component, i.e. $b_z \neq 0$. The growth rates of the diffusion modes are shown in Figure 6. These diffusion modes have a preference for $k_\perp \gg k_\parallel$ but they have zero growth rate if $k_\parallel = 0$. Interestingly, they grow on a smaller length scale than the diffusion modes found for $d\ln\mu/d\ln P < 0$. This type of atmosphere (isothermal with the mean molecular weight decreasing with height) is relevant in the context of the boundary between the intermediate and the outer ICM in the model of Peng & Nagai (2009) that we discuss next.

6. APPLICATIONS TO SEDIMENTATION MODELS

Having gained some insight into the various instabilities that can be triggered by the presence of a composition gradient in an isothermal environment, we now address the stability properties of more realistic scenarios, relevant to the conditions expected in the ICM. In order to accomplish this, we consider one of the models for Helium sedimentation introduced in Peng & Nagai (2009). Before we present the analysis of the stability of a cluster model in which Helium has sedimented efficiently, we provide a brief summary of the assumptions and procedure involved in deriving these models.

6.1. *Spherically Symmetric Helium Sedimentation Models*

In the He sedimentation model of Peng & Nagai (2009) the plasma is assumed to be in hydrostatic equilibrium in the gravitational potential that is mainly due to dark matter. The composition is initially uniform with $c = 0.25$ ($\mu = 0.59$) at all radii as given by the primordial abundance of Helium. The temperature of the cluster has a radial dependence that is motivated by observations and it is fixed in time. This amounts to assuming that heating and cooling are balanced at all radii. This assumption is also made, for instance, in Shtykovskiy & Gilfanov (2010b). Furthermore, because the stellar mass content of a cluster is smaller than the total Helium mass, enrichment from galaxies can be ignored (Markevitch 2007).

Given this initial setup, the Burgers' equations (Burgers 1969; Thoul et al. 1994) are solved for each ion species of the plasma assumed to consist of Hydrogen and Helium ions, as well as electrons. The diffusion velocity of the Helium ions is found by assuming that the gravitational force on the Helium ions is balanced by the force due to electric fields, the gradient in partial pressure and resistance due to collisions with Hydrogen ions. The result is a slow gravitational settling of Helium ions toward the core and the development of a non-uniform composition profile. This change in the composition of the gas takes the cluster out of hydrostatic equilibrium. This is caused by the change in the pressure which depends on the mean molecular weight, μ, see Equation (8). Burgers' equations only describe the relative motion of the species and so a momentum equation for the bulk flow of the gas needs to be solved in order to describe the restoration of hydrostatic equilibrium. The radial distribution of Hydrogen and Helium is evolved by repeating these steps over cosmological timescales.

6.2. *Evolving the Composition in Sedimentation Models*

A brief summary of the calculations involved in the models described in detail in Peng & Nagai (2009) can be outlined as follows.

The total density distribution (gas + dark matter) of the cluster is given by the Navarro-Frenk-White profile (Navarro

et al. 1997)

$$\rho_{\rm tot}(r) = \frac{\rho_s}{r/r_s(1+r/r_s)^2}\,, \tag{48}$$

where ρ_s is a normalization constant and r_s is a characteristic scale. The total mass, $M(r)$, enclosed within the radius, r, can be found by integrating the density distribution. This yields

$$M(r) = 4\pi\rho_s r_s^3\left[\ln(1+r/r_s) - \frac{r/r_s}{1+r/r_s}\right]\,, \tag{49}$$

from which one can find the gravitational acceleration at a distance r

$$g(r) = \frac{GM(r)}{r^2}\,, \tag{50}$$

where G is the gravitational constant.

As per convention, r_{500} (r_{2500}) is defined to be the radius inside of which the mean density is 500 (2500) times the critical density of the universe. The value of r_s is chosen such that $r_s = 0.25r_{500}$. The model presented here has $r_{500} = 1.63$ Mpc, $r_{2500} = 0.75$ Mpc and a total cluster mass, $M(r_{500}) = 1.24\times10^{15}\ M_\odot$ where $M_\odot$ is the solar mass. The ratio of the mass of the ICM to the total mass of the cluster is assumed to be 0.15 at r_{500}. The temperature profile is given by

$$\frac{T(r)}{T_0} = \frac{(r/0.045r_s)^{1.9}+0.45}{(r/0.045r_s)^{1.9}+1}\frac{1.216}{[1+(r/0.6r_s)^2]^{0.45}}, \tag{51}$$

where $T_0 = 10$ keV. The parameters used in the model and the functional dependence of $T(r)$ are motivated by a Chandra sample of 13 nearby, relaxed galaxy clusters (Vikhlinin et al. 2006). The density, ρ, and pressure, P, of the gas is found by solving the equation of hydrostatic equilibrium

$$\frac{dP}{dr} = -\rho g(r)\,, \tag{52}$$

where the gravitational potential is given by Equation (50) and the pressure is related to the density by Equation (8).

Burgers' equations, namely the continuity and momentum equations for each species, s, are given by (Burgers 1969; Thoul et al. 1994)

$$\frac{\partial n_s}{\partial t} + \frac{1}{r^2}\frac{\partial(r^2 n_s u_s)}{\partial r} = 0\,, \tag{53}$$

$$\frac{\partial P_s}{\partial r} + n_s A_s m_{\rm H} g - n_s Z_s e E = \sum_t K_{st}(w_t - w_s)\,. \tag{54}$$

where n_s is the number density, u_s is the velocity, and w_s is the velocity of species s relative to the bulk velocity of the fluid, u. The mass and charge numbers of ion species s are given by A_s and Z_s. The electric field is given by E and the resistance coefficients are given by

$$K_{st} = f_{\rm B}^{-1}\frac{4\sqrt{2\pi}}{3}\frac{e^4 Z_s^2 Z_t^2 m_{st}^{1/2}}{(k_{\rm B}T)^{3/2}} n_s n_t \ln\Lambda_{st}\,, \tag{55}$$

where m_{st} is the reduced mass and $\ln\Lambda_{st}$ is the Coulomb logarithm of species s and t, which we set to 40 (see more details in Appendix B). The parameter $f_{\rm B}^{-1}$ is the magnetic suppression factor that regulates the slow down of the sedimentation process envisioned to arise as a result of tangled magnetic fields. The profiles shown in Figure 7 have been obtained by setting $f_{\rm B} = 1$ and thus ignore this effect.

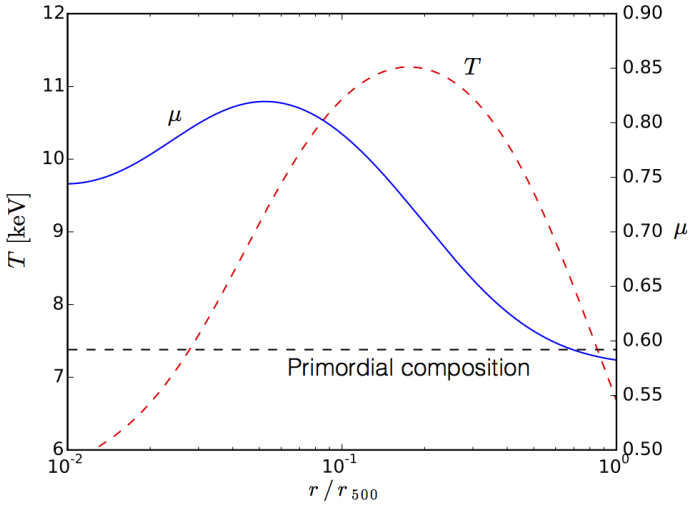

Figure 7. The mean molecular weight profile (blue line) in a 11 Gyr-old galaxy cluster and the temperature profile (red dashed line) used in the model of Peng & Nagai (2009). The dashed black line indicates the primordial composition at $t = 0$ Gyr which is $\mu = 0.59$.

Burgers' equations are solved along with the momentum equation for the bulk motion of the gas

$$\rho\frac{du}{dt} = -\frac{\partial P}{\partial r} - \rho g(r)\,, \tag{56}$$

and the distribution of elements is found as a function of time.

We show the results from a calculation using this method in Figure 7 which was produced by rerunning the code[3] developed by Peng & Nagai (2009). In this figure, the mean molecular weight profile for a 11 Gyr-old cluster is shown along with the temperature profile used for the calculation. A simple explanation of the peak in the mean molecular weight is that the resistance coefficient depends strongly on temperature. This means that He sedimentation will tend to be most effective where the temperature is high. The dashed black line shows the initial (primordial) composition of the plasma.

Efficient sedimentation in the ICM can lead to biases in the estimates of key parameters of clusters if the sedimentation is not taken into account in the data analysis. The specific model described here would lead to biases of 6% in the total mass and gas mass at $r = r_{2500}$ if a homogeneous plasma is assumed. This would create a bias of 12% in the gas mass fraction of the cluster and a bias of around 20% in the estimate for the Hubble constant (see Figure 4 in Peng & Nagai 2009). In the next section we discuss how the composition profile inferred from the model could be unstable at all radii due to plasma instabilities.

6.3. *Stability Analysis of Helium Sedimentation Models*

The model presented in Peng & Nagai (2009) provides estimates for the derivatives $d\ln T/d\ln P$ and $d\ln\mu/d\ln P$ as a function of radius. This is illustrated in Figure 8, where we have divided the ICM into three regions. The inner

[3] The authors of Peng & Nagai (2009) kindly provided us with a copy of the original Fortran code used for their paper.

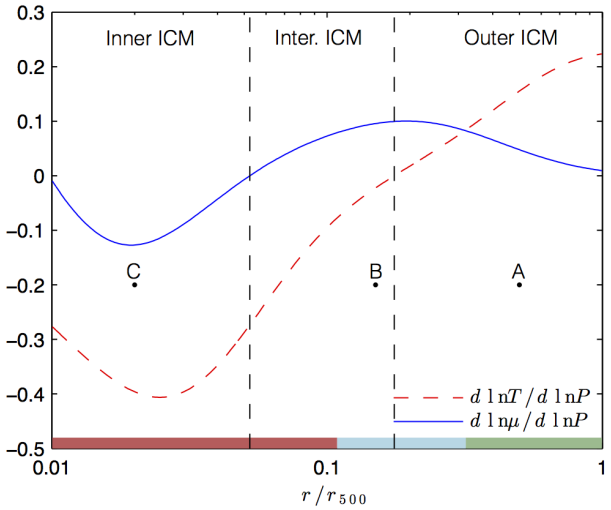

Figure 8. The gradients $d\ln T/d\ln P$ (red dashed line) and $d\ln\mu/d\ln P$ (blue line) as a function of radius in the model of Peng & Nagai (2009) at $t = 11$ Gyr. The ICM is divided into inner ICM, intermediate ICM and outer ICM. The color bar illustrates which instabilities could be triggered, see Figure 9 for the color coding. The labels A, B and C indicate the radii used to produce Figure 11, 12 and 13.

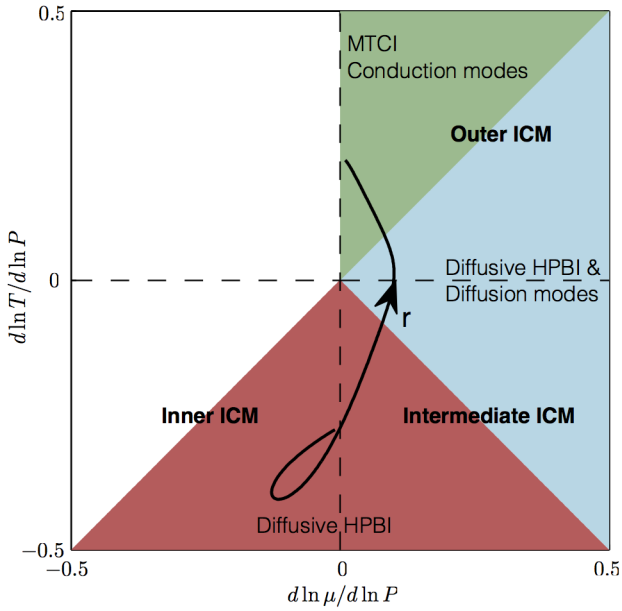

Figure 9. Parametric plot in the $(d\ln\mu/d\ln P, d\ln T/d\ln P)$ plane as a function of r/r_{500} (black line with arrow indicating the direction of increasing radial distance). Red is unstable to the diffusive HPBI. Blue is unstable to the diffusive HPBI and the diffusion modes. Green is unstable to the MTCI and the conduction modes. Comparing this figure with the stability diagrams of Pessah & Chakraborty (2013) leads to the color bars identifying the different regions in Figure 8.

ICM which extends from $r/r_{500} = 0.01$ to the radius where $d\ln\mu/d\ln P = 0$ ($r/r_{500} = 0.05$) and the outer ICM which extends from the radius where $d\ln T/d\ln P = 0$ ($r/r_{500} = 0.18$) to the radius $r/r_{500} = 1$. The intermediate ICM is defined to be the region in between the previous two.

Before delving into details, we can provide a qualitative idea about which parts of the ICM are prone to the different types of instabilities. In order to do this, we consider the numerical values of the gradients in temperature and composition in the context of the stability diagrams introduced in Pessah & Chakraborty (2013) (see Figure 2 and 3 in their paper). The comparison is facilitated by using a parametric plot in the $(d\ln\mu/d\ln P, d\ln T/d\ln P)$ plane, see Figure 9. The colored sections in this figure indicate the regions of parameter space which are subject to the different types of instabilities discussed in Section 4. The extent of these regions is also indicated with color bars at the bottom of Figure 8. The red color bar indicates the region where the diffusive HPBI could be active and the blue bar indicates the region where the diffusive HPBI and the diffusion modes could be active. Finally, the region highlighted by the green bar is unstable to the MTCI and the conduction modes.[4] These conclusions require, of course, that the magnetic field geometry allows for the various instabilities to be triggered.

The stability criteria derived in Pessah & Chakraborty (2013) assume that magnetic tension is negligible. In order to assess whether this effect could be important, we need a model for the magnetic field strength in the ICM. We can estimate the plasma β as a function of cluster radius, $\beta(r)$, for the model of Peng & Nagai (2009), by using

$$B(r) = B_0 \left(\frac{n_e(r)}{n_e(0)}\right)^{\eta}, \qquad (57)$$

where n_e is the electron number density, $B_0 = 4.7\ \mu$G, and $\eta = 0.5$, as found for the Coma cluster in Bonafede et al. (2010). The quantitative results therefore depend on this choice while the qualitative results should not. Using this model, we illustrate in Figure 10 the potential role that magnetic tension could play, especially in the inner parts of the ICM. The assumptions made in Pessah & Chakraborty (2013) are valid within region 4 in Figure 10. The dispersion relation derived in this paper extends the validity of the analysis to also include regions 2 and 5 where magnetic tension is important. For the sake of completeness, we recall that the fluid approximation breaks down in region 1 and 3 and that the local approximation in the linear analysis breaks down in region 6 and 7.

In what follows, we discuss the growth rates and the characteristic distances on which the various instabilities could operate in the cluster model of Peng & Nagai (2009) at $t = 11$ Gyr. Using the radial profiles provided by the model, we can calculate the values of the needed parameters ($d\ln T/d\ln P$, $d\ln\mu/d\ln P$, $\omega_{\rm dyn}$, H, $\lambda_{\rm mfp}$, Kn, $\chi_\parallel$, $\nu_\parallel$, D) as a function of radius. In addition to the model of Peng & Nagai (2009) we consider a magnetic field given by Equation (57) to estimate β.

In order to assess the influence of the sedimentation of Helium on the stability properties of the ICM we solve the dispersion relation for the sedimentation model of Peng & Nagai (2009) at both $t = 0$ Gyr and $t = 11$ Gyr. We include anisotropic heat conduction, Helium diffusion, Braginskii viscosity and a finite β in the calculations in Section 6.4, 6.5 and 6.6. The effect of Braginskii viscosity is to damp perturbations with short perpendicular wavelengths. The effect of the magnetic tension is to stabilize modes with short parallel wavelengths and, in general, to inhibit the growth rates. The role of magnetic tension in decreasing the maximum growth rate is investigated in Section 7. In the following we consider

[4] The conduction modes are important in the slow conduction limit, $\omega_c \ll \omega_{\rm dyn}$, see Pessah & Chakraborty (2013).

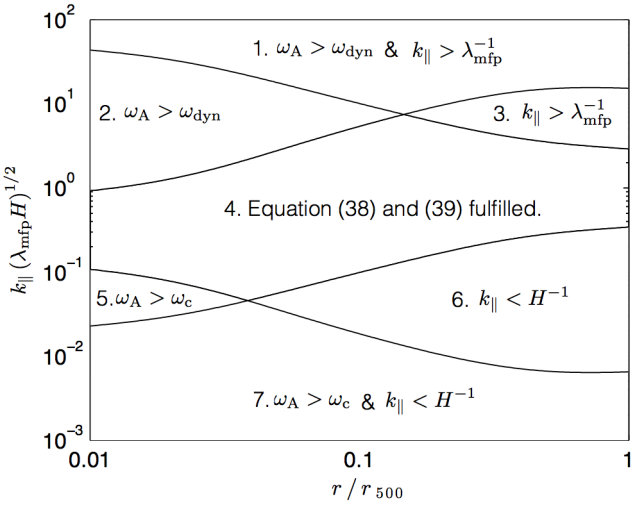
1. $\omega_A > \omega_{dyn}$ & $k_\parallel > \lambda_{mfp}^{-1}$
2. $\omega_A > \omega_{dyn}$
3. $k_\parallel > \lambda_{mfp}^{-1}$
4. Equation (38) and (39) fulfilled.
5. $\omega_A > \omega_c$
6. $k_\parallel < H^{-1}$
7. $\omega_A > \omega_c$ & $k_\parallel < H^{-1}$
$k_\parallel (\lambda_{mfp} H)^{1/2}$
r / r_{500}

Figure 10. Validity of the local linear analysis as a function of radius. The results of Pessah & Chakraborty (2013) are valid within region 4. The effects of magnetic tension should be accounted for in regions 2 and 5. The fluid approximation breaks down in region 1 and 3 and the local approximation breaks down in region 6 and 7.

each of the three regions of the ICM defined in Figure 8 separately.

6.4. *Outer ICM*

In the model of Peng & Nagai (2009) at $t = 11$ Gyr, both the temperature and the mean molecular weight decrease with radial distance in the outer ICM, as illustrated in Figure 7. In the inner part of the outer ICM we have $d\ln\mu/d\ln P > d\ln T/d\ln P$, see Figure 8, and this makes this region unstable to diffusion driven modes and the diffusive HPBI at short parallel wavelengths and to the diffusion modes at long parallel wavelengths. In the outer part of the outer ICM we have $d\ln\mu/d\ln P < d\ln T/d\ln P$ which makes this region unstable to the MTCI and to conduction modes at long parallel wavelengths. The model at $t = 0$ Gyr, before Helium has had time to sediment, is unstable to the MTI. We note that these conclusions depend on the magnetic field geometry.

As an illustration, we consider a magnetic field inclined at $\theta = 45°$ at a specific radial distance, $r/r_{500} = 0.5$, indicated with a letter A on Figure 8. Using values evaluated at this location ($d\ln T/d\ln P = 0.16$ and $d\ln\mu/d\ln P = 0.05$ at $t = 11$ Gyr and $d\ln T/d\ln P = 0.16$ and $d\ln\mu/d\ln P = 0$ at $t = 0$ Gyr) we calculate the growth rates, as shown in Figure 11. In the panel on the left (right) we show the growth rate as a function of wavenumber for the model at $t = 0$ Gyr ($t = 11$ Gyr). We observe that the maximum growth rate is $\sigma \approx 0.87$ Gyr^{-1} without Helium sedimentation ($t = 0$ Gyr) and $\sigma \approx 0.75$ Gyr^{-1} with Helium sedimentation ($t = 11$ Gyr) such that the instabilities grow unstable on a timescale of either 1.15 Gyr or 1.3 Gyr, respectively. The presence of Helium sedimentation is concluded to lead to a decrease in the growth rate by approximately 15%, in agreement with the rough estimate in Pessah & Chakraborty (2013). Considering a characteristic scale $L = 2\pi/k$, the fastest growing mode corresponds to $(L_x, L_z) = (1.0, 1.0)$ Mpc at $t = 0$ Gyr. This scale is slightly decreased to $(L_x, L_z) = (0.9, 0.8)$ Mpc at $t = 11$ Gyr. The unstable modes found are describable by a fluid approach (at this radial distance $\lambda_{mfp} = 30$ kpc) but they are

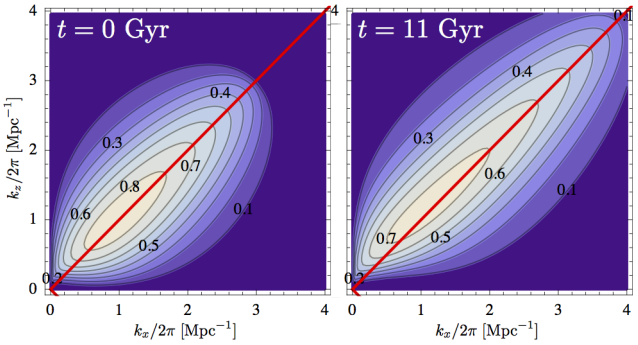

Figure 11. Contour plots of the growth rate in Gyr^{-1} for the outer ICM (location C). This region is unstable to the MTI at $t = 0$ Gyr (left panel) or the MTCI and the conduction modes at $t = 11$ Gyr (right panel). The most unstable modes are found at intermediate parallel wavenumbers because magnetic tension stabilizes modes with a high parallel wavenumber. The maximum growth rate is decreased by 15% with respect to the homogeneous case.

not strictly describable by a local linear analysis (at this radial distance $H = 0.35$ Mpc). The value of ω_{dyn}^{-1} at this distance is roughly 0.3 Gyr so the instability grows on a timescale a factor of a few larger than the dynamical timescale.

6.5. *Intermediate ICM*

According to the model at $t = 11$ Gyr, the temperature increases while the mean molecular weight decreases with radial distance in the intermediate ICM. The stability diagrams of Pessah & Chakraborty (2013) then reveal that the intermediate ICM is unstable to the diffusive HPBI in the entire region. Furthermore, the outer part of the intermediate ICM is unstable to the diffusion modes.

For illustrative purposes, we consider the radial distance indicated with a letter B on Figure 8 which is located at $r/r_{500} = 0.15$. At this location, $d\ln T/d\ln P = -0.02$ and $d\ln\mu/d\ln P = 0.1$ at $t = 11$ Gyr and so the diffusion modes and the diffusive HPBI are expected to be active. In the absence of sedimentation this radial distance is unstable to the HBI ($d\ln T/d\ln P = -0.03$ and $d\ln\mu/d\ln P = 0$ at $t = 0$ Gyr). We consider the growth rates for the $t = 0$ Gyr cluster in the left panel and the $t = 11$ Gyr in the right panel of Figure 12. In this figure we have assumed $\theta = 75°$. The intermediate region is stabilized by the gradient in composition at $t = 11$ Gyr if anisotropic particle diffusion is neglected ($D = 0$) but when anisotropic particle diffusion is taken into account ($D \neq 0$) the diffusive HPBI and diffusion modes could be active. This can understood from the criteria for stability for the HPBI, the diffusive HPBI and the diffusion modes, given by Equations (45), (46) and (47), respectively. While Equation (45) is satisfied Equations (46) and (47) are not. We conclude that even though diffusion modes only grow on a diffusive timescale, ω_D^{-1}, they can be dominant if the instabilities that grow on a conduction timescale, ω_c^{-1}, are not active. The diffusive HPBI, however, requires that $\omega_D \gg \omega_{dyn}$, a requirement that is not fulfilled in the unstable region in Figure 12. The diffusion modes are active regardless of whether $\omega_D \gg \omega_{dyn}$ or $\omega_D \ll \omega_{dyn}$, and so the growth rates present in Figure 12 are interpreted to be due to the diffusion modes. The maximum growth rates are $\sigma \approx 0.28$ Gyr^{-1} at $t = 0$ Gyr and $\sigma \approx 0.59$ Gyr^{-1} at $t = 11$ Gyr corresponding to time scales of 3.6 Gyr and 1.7 Gyr, respectively. The maximum growth rate

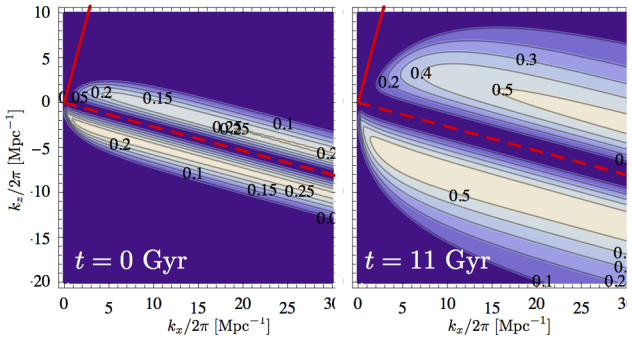

Figure 12. Contour plots of the growth rate in Gyr^{-1} for the intermediate ICM (location B). This region is unstable to the HBI at $t = 0$ Gyr (left panel) or the diffusion modes and the diffusive HPBI at $t = 11$ Gyr (right panel). This region is only unstable at $t = 11$ Gyr if $D \neq 0$. The maximum growth rate is increased with 110% with respect to the homogeneous case.

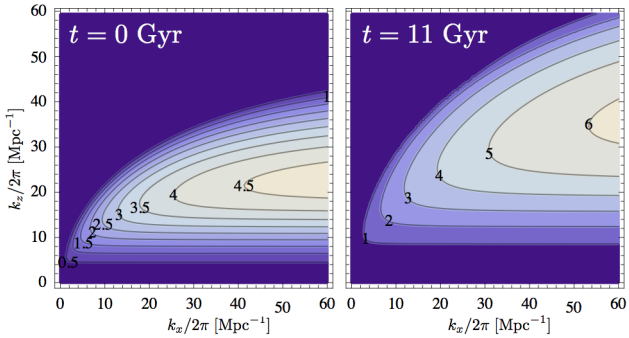

Figure 13. Contour plots of the growth rate in Gyr^{-1} for the inner ICM (location A). This region is unstable to the HBI at $t = 0$ Gyr (left panel) and to the diffusive HPBI at $t = 11$ Gyr (right panel). In both cases, the maximum growth rate is significantly decreased and the most unstable modes are found at longer parallel wavelengths because of magnetic tension. The maximum growth rate is increased by 40% with respect to the homogeneous case.

is increased by 110% with respect to the homogeneous case. The most unstable scales are $(L_x, L_z) = (0.32, 0.35)$ Mpc at $t = 0$ Gyr and $(L_x, L_z) = (0.15, 0.15)$ Mpc at $t = 11$ Gyr.

6.6. *Inner ICM*

In the inner ICM both the temperature and the mean molecular weight increase with radial distance at $t = 11$ Gyr. This implies that this region is only unstable with respect to the diffusive HPBI at $t = 11$ Gyr. At $t = 0$ Gyr, it is unstable to the HBI. The magnetic field strength increases towards the center of the ICM and so we expect the magnetic tension to dampen the growth rates more severely in the inner ICM.

We consider the radial distance indicated with a letter C on Figure 8, which is located at $r/r_{500} = 0.02$. At this radius, $d\ln T/d\ln P = -0.4$, $d\ln\mu/d\ln P = -0.13$ at $t = 11$ Gyr and $d\ln T/d\ln P = -0.51$, $d\ln\mu/d\ln P = 0$ at $t = 0$ Gyr. Due to the low value of βKn ≈ 2, we expect magnetic tension to influence the dynamics as highlighted in Figure 13. We assume that $\theta = 90°$ which is the maximally unstable configuration. In Figure 13, the left panel shows the growth rates at $t = 0$ Gyr and the right panel shows the growth rates at $t = 11$ Gyr. Braginskii viscosity makes the HPBI have a preference for $k_\perp \gg k_\parallel$, as explained in Section 5. Magnetic tension also acts to inhibit the growth of modes with a high parallel wavenumber. Braginski viscosity and magnetic tension are therefore the reasons for the zero growth rates at high vertical wavenumbers, k_z. The wavenumbers are not restricted in the x-direction (perpendicular to gravity) and so the fastest growth rates are attained for short distances in the x-direction because heat conduction is effective on short distance scales. The maximum growth rate is therefore found for $L_z \approx 25$ kpc and an even shorter length scale in the x-direction. The fluid limit is, however, only valid as long as $L_x \gg \lambda_{\rm mfp} \approx 40$ pc at this distance. The vertical length scale of the fastest growing mode should be much smaller than $H \approx 50$ kpc but this is not the case. The maximum growth rates are $\sigma \approx 5$ Gyr^{-1} without sedimentation and $\sigma \approx 7.2$ Gyr^{-1} with sedimentation corresponding to time scales for growth of 0.20 Gyr and 0.14 Gyr, respectively. When sedimentation is present, we find that the maximum growth rate is increased by 40% with respect to the homogeneous case.

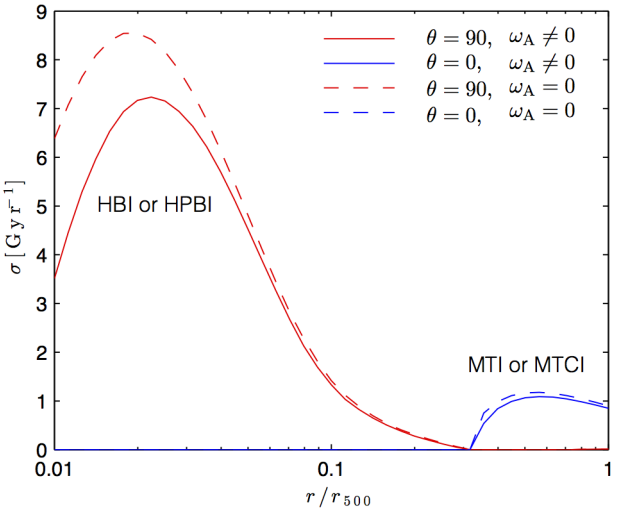

Figure 14. The maximum growth rates as a function of radius in the cluster model of Peng & Nagai (2009) at $t = 11$ Gyr in the limit where magnetic tension is neglected (dashed lines) and when it is taken into account (solid lines).

6.7. *Magnetic tension decreases the growth rates*

In order to assess how the effect of magnetic tension modifies the growth rates we compare the solutions we obtain when we set $\omega_A = 0$ with those found when we set ω_A equal to the value found by combining the model of Peng & Nagai (2009) at $t = 11$ Gyr with Equation (57). The maximum growth rates as a function of radius for a field with $\theta = 90°$ and $\theta = 0°$ inclination with respect to the direction of gravity are shown in Figure 14. The solid lines include $\omega_A \neq 0$ while the dashed lines are found by solving the $\omega_A = 0$ limit of the dispersion relation. We conclude that magnetic tension decreases the maximum growth rate at all radii but the effect is seen to be most significant in the inner cluster region (Carilli & Taylor 2002; Kunz 2011; Pessah & Chakraborty 2013).

7. DISCUSSION AND PROSPECTS

Understanding whether He sedimentation in galaxy clusters is efficient or whether it can be hindered by tangled magnetic fields, turbulence, or mergers remains an open question in astrophysics. Addressing this problem from first principles de-

mands a better understanding of the processes involved in the weakly collisional, magnetized plasma constituting the ICM. As a first step in this endeavor, we have taken a simple approach to gauge the importance of various dynamical instabilities, related to the MTI and HBI, that can feed off temperature and composition gradients (Pessah & Chakraborty 2013) as expected from state-of-the-art sedimentation models (Peng & Nagai 2009).

We have shown that if a gradient in the composition of the ICM arises due to Helium sedimentation, as modeled for example in Peng & Nagai (2009), this might not be a stable equilibrium. We illustrated this by showing that, depending on the magnetic field orientation, the radial profile of the sedimentation model is unstable, to different kinds of instabilities, at all radii. The instabilities are shown to grow on timescales that are short compared to the life-time of a typical cluster. Our findings are summarized in Figure 15 where we show the maximum growth rate as a function of radius for both the homogeneous cluster model (t = 0 Gyr) and the cluster model with a gradient in composition (t = 11 Gyr) for a magnetic field that is either parallel or perpendicular to the direction of gravity. In this figure we find that, in accordance with Pessah & Chakraborty (2013), Helium sedimentation can lead to an increase in the maximum growth rate in the inner cluster region but a decrease in the maximum growth rate in the outer cluster region. The figure illustrates that the composition gradients, as inferred from sedimentation models which do not fully account for the weakly collisional character of the environment, are not necessarily robust even though the entropy increases with radius. This contrasts the arguments regarding the stability of composition gradients put forth in Markevitch (2007), which predates the discovery of the HBI (Quataert 2008).

The instabilities discussed in this paper could provide an efficient mechanism for diminishing the mean molecular weight gradient in the ICM by turbulently mixing the Helium content. Whether this is the case depends on how the instabilities saturate as well as the large scale dynamical processes that contribute to determining the global gradient in the mean molecular weight. There are several processes that could play a role in this regard at both small and large scales. Understanding their influence will lead to a more realistic picture of the ICM dynamics. We mention a few examples below.

The equations of kinetic MHD used in this paper do not incorporate the physics responsible for the composition gradients found in sedimentation models based on Burger's equations. They are therefore not able to self-consistently describe the coupling of magnetic fields to the sedimentation process. One possible route forward would be to extend the equations of kinetic MHD and take the sedimentation process into account by following Bahcall & Loeb (1990). This would allow us to describe the dynamical influence of the magnetic field at the cost of using a one-fluid model instead of the commonly used multifluid models. Even though an extension of the kinetic MHD framework would describe unmagnetized sedimentation less precisely than Burgers' equations (Thoul et al. 1994), this would be a step forward in our understanding of sedimentation processes in the ICM.

Our idealized model of the ICM consisted of a weakly collisional, plane-parallel atmosphere in hydrostatic equilibrium. Real clusters are most likely not in perfect hydrostatic equilibrium as the ICM can be stirred by mergers and accretion.

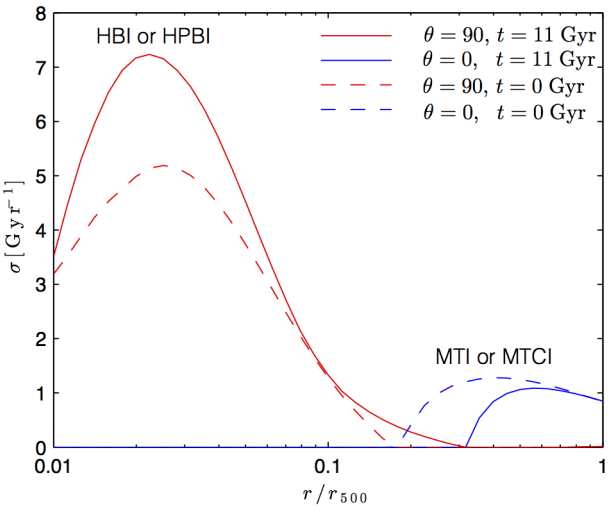

Figure 15. The maximum growth rate as a function of radius in the cluster model of Peng & Nagai (2009) at t = 0 (dashed) and t = 11 Gyr (solid) for a field with $\theta = 90°$ (red) and $\theta = 0°$ (blue) inclination with respect to the direction of gravity. The effects of a finite β are included. The sedimentation increases (decreases) the theoretically predicted growth rates in the inner (outer) cluster.

The ensuing turbulence can contribute with a significant fraction of the pressure support needed to counteract gravity (Lau et al. 2009; Nelson et al. 2014). The instabilities we have described could be influenced by such turbulence, as well as by the cosmological expansion over timescales comparable to the age of the Universe (Ruszkowski et al. 2011).

Another issue raised in this paper is that some of the fastest growing modes grow on scales that are not strictly local in height. This means that there is a need for a quasi-global theory as developed in Latter & Kunz (2012) in order to correctly describe the linear dynamics of the weakly collisional medium. Other issues may affect the plasma dynamics at small scales. Very fast microscale instabilities, such as the firehose and mirror instabilities, could play a key role in the ICM (Schekochihin & Cowley 2006; Schekochihin et al. 2010; Kunz et al. 2011). These instabilities are not correctly described in the framework of kinetic MHD (Schekochihin et al. 2005). This might not be a problem if the microinstabilities saturate in such a way that they drive the pressure anisotropy to marginal stability (Schekochihin et al. 2008; Rosin et al. 2011). This is still an outstanding issue in the study of homogeneous plasmas. The microinstabilities are not a concern for the linear evolution of the MTI and the HBI but they are important for simulations of their nonlinear evolution (Kunz et al. 2012). We anticipate the need to deal with similar issues for simulations of the nonlinear evolution of the instabilities that are driven by gradients in composition.

We are grateful to Daisuke Nagai and Fang Peng for giving us a copy of their Fortran code that we used to reproduce the data in their sedimentation model. We are grateful to the anonymous referee for a thoughtful and detailed report. The suggestion to make a more comprehensive comparison between a homogeneous and a heterogeneous ICM inspired us to produce several new figures and helped us to significantly improve the final version of this manuscript. We acknowledge useful discussions with Daisuke Nagai, Matthew Kunz,

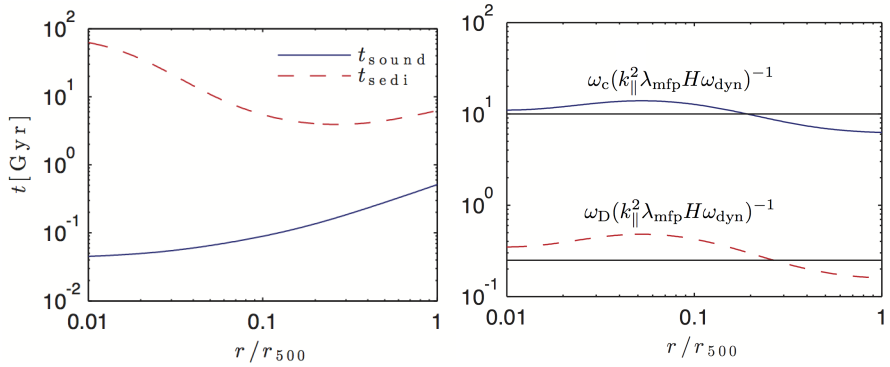

Figure 16. *Left:* The timescale for sedimentation across a scale height (red dashed) and the timescale for sound to cross a scale height (blue) as a function of radius in the model of Peng & Nagai (2009). *Right:* The dimensionless values of $\omega_{\rm c}$ (blue) and $\omega_{\rm D}$ (red dashed) are shown as a function of radius. The approximations given in Equations (35) and (37) are indicated with solid horizontal lines.

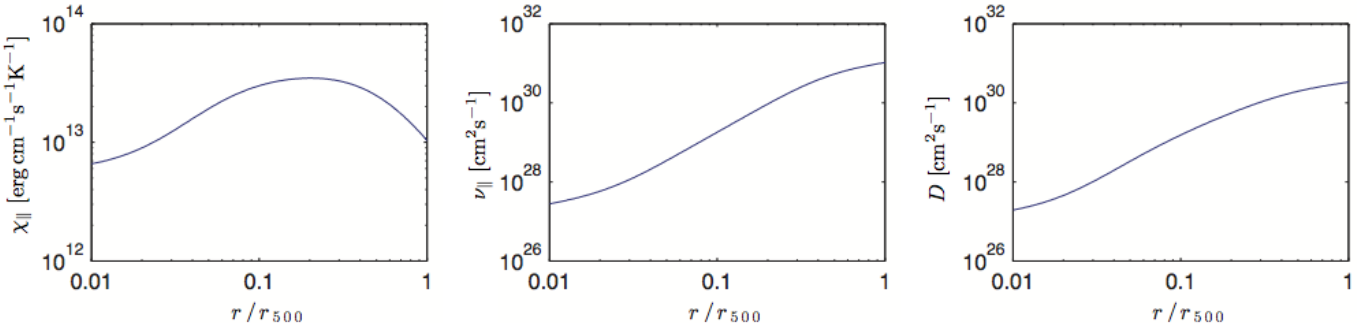

Figure 17. The values of $\chi_\parallel$ (left), $\nu_\parallel$ (middle) and D (right) as function of radius in the cluster model of Peng & Nagai (2009) at $t = 11$ Gyr.

Prateek Sharma, Ellen Zweibel, and Ian Parrish during the 3rd *ICM Theory and Computation Workshop* held at the Niels Bohr Institute in 2014. We also thank Sagar Chakraborty and Henrik Latter for valuable comments. The research leading to these results has received funding from the European Research Council under the European Union's Seventh Framework Programme (FP/2007-2013) under ERC grant agreement 306614. T. B. also acknowledges support provided by a Lørup Scholar Stipend and M. E. P. also acknowledges support from the Young Investigator Programme of the Villum Foundation.

APPENDIX

A. CHARACTERISTIC TIME SCALES FOR SEDIMENTATION AND ANISOTROPIC TRANSPORT

A.1. *Helium sedimentation*

In this paper we have built on the stability analysis of Pessah & Chakraborty (2013) and applied these tools to the Helium profile provided by the sedimentation model of Peng & Nagai (2009) in order to calculate the growth rates of instabilities that could be present in this model of the ICM. In our calculations we have assumed that the composition profiles evolve on timescales that are longer than the characteristic timescales in which the instabilities operate. Within this framework, we found that the relevant instabilities grow on timescales comparable to the dynamical timescale. We show here that our approach is justified because the timescales involved in the sedimentation process are much longer than the dynamical timescale. In order to estimate the timescale for sedimentation, we use an approximation for the sedimentation velocity, $w_{\rm He}$, given by

$$w_{\rm He} \simeq 80\,{\rm km\,s^{-1}}\left(\frac{T}{10\,{\rm keV}}\right)^{3/2}\left(\frac{g}{10^{-7.5}\,{\rm cm\,s^{-2}}}\right) \times\left(\frac{n_{\rm H}}{10^{-3}{\rm cm^{-3}}}\right)^{-1}, \tag{A1}$$

in Peng & Nagai (2009) for a single Helium ion immersed in a Hydrogen background. Here, $n_{\rm H}$ is the Hydrogen number density. The separation of timescales is illustrated in Figure 16 where we show the time for a He ion to sediment a distance of one scale height ($t_{\rm sedi} = H/w_{\rm He}$) along with the dynamical timescale ($t_{\rm sound} = H/v_{\rm th} = \omega_{\rm dyn}^{-1}$) as a function of radius in the cluster. We observe that the timescales differ by more than an order of magnitude, providing support to our assumption.

A.2. *Heat conduction, Braginskii viscosity and particle diffusion*

In order to estimate the timescale for particle diffusion we use Equations (B6), (B7) and (B8) to estimate the coefficients $\chi_\parallel$, $\nu_\parallel$ and D. We calculate the dimensionless values of $\omega_{\rm c}$, $\omega_{\rm v}$ and $\omega_{\rm D}$ by scaling them with $k_\parallel^2\lambda_{\rm mfp}H\omega_{\rm dyn}$ where the frequencies $\omega_{\rm c}$, $\omega_{\rm v}$ and $\omega_{\rm D}$ are defined in Equation (24). The dimensionless values of $\omega_{\rm c}$ and $\omega_{\rm D}$ are shown as a function of radius (using the model of Peng & Nagai 2009) in the right panel of Figure 16. From this figure we estimate that the diffusion timescale is roughly 40 times longer than the timescale for heat conduction, enabling us to estimate $\omega_{\rm D}$ as in Equation (37). The dimensionless value of $\omega_{\rm v}$ does not depend on any physical parameters and is therefore 3/2 at all radii.

B. TRANSPORT PROPERTIES OF A HYDROGEN-HELIUM PLASMA

The procedure used to derive the kinetic MHD equations for a binary mixture is similar to the procedure used for a pure Hydrogen plasma (Braginskii 1965; Kulsrud 1983).

The non-ideal transport coefficients for a plasma consisting of Hydrogen and Helium ions as well as electrons are found by using the Krook operator in the Vlasov-Landau-Maxwell equations

$$\frac{\partial f_s}{\partial t} + \boldsymbol{v}\cdot\boldsymbol{\nabla} f_s + \left[\frac{q_s}{m_s}\left(\boldsymbol{E} + \frac{\boldsymbol{v}\times\boldsymbol{B}}{c}\right) + \boldsymbol{g}\right]\cdot\frac{\partial f_s}{\partial \boldsymbol{v}} = C[f_s]\ . \quad \text{(B1)}$$

Here, f_s is the one-particle phase-space distribution of species s and q_s (m_s) is the particle charge (mass). The Krook operator is given by (Snyder et al. 1997)

$$C[f_s] = -\sum_t \nu_{st}\,(f_s - F_{Mst})\ , \quad \text{(B2)}$$

where the sum extends over all species and the equilibrium function, F_{Mst}, is given by

$$F_{Mst} = \frac{n_s}{(2\pi T_s/m_s)^{3/2}}\exp\left[-\frac{m_s}{2T_s}\left(v_\parallel - u_{\parallel,t}\right)^2 - \frac{m_s}{2T_s}v_\perp^2\right]\ . \quad \text{(B3)}$$

Here, the collision frequency between species s and t is given by

$$\nu_{st} = \frac{4\sqrt{2\pi}}{3}\frac{n_t m_{st}^{1/2} e^4 (Z_s Z_t)^2}{m_s (k_{\rm B}T)^{3/2}}\ln\Lambda_{st}\ , \quad \text{(B4)}$$

where $\ln\Lambda_{st}$ is the Coulomb logarithm and

$$m_{st} = \frac{m_s m_t}{m_s + m_t}\ , \quad \text{(B5)}$$

is the reduced mass. Furthermore, the mean velocity in the parallel direction of species s is $u_{\parallel,s}$ and we assume that all species have the same temperature, $T_s = T$.

Following Peng & Nagai (2009), Shtykovskiy & Gilfanov (2010a) we use $\ln\Lambda_{st} = 40$ which is a characteristic value for the ICM. One can derive the kinetic MHD equations, given by Equations (1)-(4), by assuming that the distribution function is gyrotropic and calculating moments in velocity space of the Landau-Vlasov equation (Kulsrud 1983). If it is assumed that the distribution function is Gaussian when calculating the moments $v_\parallel^4$, $v_\perp^4$, and $v_\parallel^2 v_\perp^2$, the equations are closed and one can show that (see, for instance, A. A. Schekochihin & M. W. Kunz, in preparation)

$$\chi_\parallel = \frac{5}{2}\frac{k_{\rm B}}{\nu_{\rm e-e} + \nu_{\rm e-H} + \nu_{\rm e-He}}\frac{P_e}{m_e}\ , \quad \text{(B6)}$$

for the heat conductivity and

$$\nu_\parallel = \frac{1}{\rho}\left(\frac{n_{\rm He}}{\nu_{\rm He-H} + \nu_{\rm He-He}} + \frac{n_{\rm H}}{\nu_{\rm H-H} + \nu_{\rm H-He}}\right)k_{\rm B}T\ , \quad \text{(B7)}$$

for the Braginskii viscosity. In these expressions the heat conduction due to ions and the viscosity due to electrons is neglected. This approximation is good because $m_{\rm H}$, $m_{\rm He} \gg m_{\rm e}$.

The anisotropic diffusion coefficient due to a gradient in the composition was approximated by Bahcall & Loeb (1990). In terms of the ratio of the Helium density to the total gas density, c, it can be expressed as (Pessah & Chakraborty 2013)

$$D = \frac{3}{16}\sqrt{\frac{5m_{\rm H}}{2\pi}}\frac{(k_B T)^{5/2}}{e^2\rho\ln\Lambda_{\rm H-He}}\left[\frac{4-c}{(2-c)(8-5c)}\right]\ . \quad \text{(B8)}$$

Using the model of Peng & Nagai (2009), we show the transport coefficients as a function of radius in Figure 17.

REFERENCES

Bahcall, J. N., & Loeb, A. 1990, ApJ, 360, 267
Balbus, S. A. 2000, ApJ, 534, 420
—. 2001, ApJ, 562, 909
Bogdanović, T., Reynolds, C. S., Balbus, S. A., & Parrish, I. J. 2009, ApJ, 704, 211
Bonafede, A., Feretti, L., Murgia, M., et al. 2010, A&A, 513, A30
Braginskii, S. 1965, Review of Plasma Physics
Bulbul, G. E., Hasler, N., Bonamente, M., et al. 2011, A&A, 533, 6
Burgers, J. M. 1969, Flow Equations for Composite Gases
Carilli, C. L., & Taylor, G. B. 2002, ARA&A, 40, 319
Chuzhoy, L., & Loeb, A. 2004, MNRAS, 349, L13
Chuzhoy, L., & Nusser, A. 2003, MNRAS, 342, L5
Fabian, A. C., & Pringle, J. E. 1977, MNRAS, 181, 5P
Gilfanov, M. R., & Syunyaev, R. A. 1984, Soviet Astronomy Letters, 10, 137
Kulsrud, R. M. 1983, in Basic Plasma Physics: Selected Chapters, Handbook of Plasma Physics, Vol. 1, ed. A. A. Galeev & R. N. Sudan, 1
Kunz, M. W. 2011, Monthly Notices of the Royal Astronomical Society, 417, 602
Kunz, M. W., Bogdanović, T., Reynolds, C. S., & Stone, J. M. 2012, The Astrophysical Journal, 754, 122
Kunz, M. W., Schekochihin, A. A., Cowley, S. C., Binney, J. J., & Sanders, J. S. 2011, MNRAS, 410, 2446
Latter, H. N., & Kunz, M. W. 2012, MNRAS, 423, 1964
Lau, E. T., Kravtsov, A. V., & Nagai, D. 2009, ApJ, 705, 1129
Ledoux, P. 1947, ApJ, 105, 305
Mantz, A. B., Allen, S. W., Morris, R. G., et al. 2014, MNRAS, 440, 2077
Markevitch, M. 2007, ArXiv e-prints, arXiv:0705.3289
McCourt, M., Parrish, I. J., Sharma, P., & Quataert, E. 2011, MNRAS, 413, 1295
McCourt, M., Sharma, P., Quataert, E., & Parrish, I. J. 2012, MNRAS, 419, 3319
Navarro, J. F., Frenk, C. S., & White, S. D. M. 1997, ApJ, 490, 493
Nelson, K., Lau, E. T., & Nagai, D. 2014, ApJ, 792, 25
Parrish, I. J., McCourt, M., Quataert, E., & Sharma, P. 2012a, MNRAS, 422, 704
—. 2012b, MNRAS, 419, L29
Parrish, I. J., & Quataert, E. 2008, ApJL, 677, L9
Parrish, I. J., Quataert, E., & Sharma, P. 2009, ApJ, 703, 96
—. 2010, ApjL, 712, L194
Parrish, I. J., & Stone, J. M. 2005, The Astrophysical Journal, 633, 334
—. 2007, The Astrophysical Journal, 664, 135
Parrish, I. J., Stone, J. M., & Lemaster, N. 2008, ApJ, 688, 905
Peng, F., & Nagai, D. 2009, The Astrophysical Journal, 693, 839
Pessah, M. E., & Chakraborty, S. 2013, ApJ, 764, 13
Qin, B., & Wu, X.-P. 2000, ApJL, 529, L1
Quataert, E. 2008, The Astrophysical Journal, 673, 758
Rosin, M. S., Schekochihin, A. A., Rincon, F., & Cowley, S. C. 2011, MNRAS, 413, 7
Ruszkowski, M., Lee, D., Brüggen, M., Parrish, I., & Oh, S. P. 2011, ApJ, 740, 81
Ruszkowski, M., & Oh, S. P. 2010, ApJ, 713, 1332
Schekochihin, A. A., & Cowley, S. C. 2006, Astronomische Nachrichten, 327, 599, arXiv: astro-ph/0508535
Schekochihin, A. A., Cowley, S. C., Kulsrud, R. M., Hammett, G. W., & Sharma, P. 2005, The Astrophysical Journal, 629, 139
Schekochihin, A. A., Cowley, S. C., Kulsrud, R. M., Rosin, M. S., & Heinemann, T. 2008, Physical Review Letters, 100, 081301
Schekochihin, A. A., Cowley, S. C., Rincon, F., & Rosin, M. S. 2010, MNRAS, 405, 291
Schwarzschild, M. 1958, Structure and Evolution of the Stars.
Shtykovskiy, P., & Gilfanov, M. 2010a, MNRAS, 401, 1360
—. 2010b, MNRAS, 401, 1360
Snyder, P. B., Hammett, G. W., & Dorland, W. 1997, Physics of Plasmas, 4, 3974
Spitzer, L. 1962, Physics of Fully Ionized Gases
Thoul, A. A., Bahcall, J. N., & Loeb, A. 1994, ApJ, 421, 828
Vikhlinin, A., Kravtsov, A., Forman, W., et al. 2006, ApJ, 640, 691